

# Implications of the $M_w$ 9.0 Tohoku-Oki Earthquake for Ground Motion Scaling with Source, Path, and Site Parameters

Jonathan P. Stewart,<sup>a)</sup> M.EERI, Saburoh Midorikawa,<sup>b)</sup> M.EERI, Robert W. Graves,<sup>c)</sup> M.EERI, Khatareh Khodaverdi,<sup>a)</sup> S.M.EERI, Tadahiro Kishida,<sup>d)</sup> M.EERI, Hiroyuki Miura,<sup>b)</sup> M.EERI, Yousef Bozorgnia,<sup>d)</sup> M.EERI, and Kenneth W. Campbell<sup>e)</sup> M.EERI

The  $M_w$ 9.0 Tohoku-oki Japan earthquake produced approximately 2,000 ground motion recordings. We consider 1,238 three-component accelerograms corrected with component-specific low-cut filters. The recordings have rupture distances between 44 km and 1,000 km, time-averaged shear wave velocities of  $V_{S30} = 90$  m/s to 1,900 m/s, and usable response spectral periods of 0.01 sec to >10 sec. The data support the notion that the increase of ground motions with magnitude saturates at large magnitudes. High-frequency ground motions demonstrate faster attenuation with distance in backarc than in forearc regions, which is only captured by one of the four considered ground motion prediction equations for subduction earthquakes. Recordings within 100 km of the fault are used to estimate event terms, which are generally positive (indicating model underprediction) at short periods and zero or negative (overprediction) at long periods. We find site amplification to scale minimally with  $V_{S30}$  at high frequencies, in contrast with other active tectonic regions, but to scale strongly with  $V_{S30}$  at low frequencies. [DOI: 10.1193/1.4000115]

## INTRODUCTION

The  $M_w$ 9.0 Tohoku-oki earthquake occurred on 11 March 2011 off the Pacific Coast of Japan. This earthquake is associated with the subduction process of the Pacific plate beneath the North American (continental) plate at the Japan Trench, which occurs with a convergence rate of about 8–9 cm/yr. The earthquake resulted from thrust-faulting at the interface between the two plates, which has produced many large historic earthquakes, including the 1896 Meiji-Sanriku earthquake (estimated  $M_w$ 8.5) and nine events of magnitude 7 or greater in the modern instrumental era (since 1973, when the Japan Meteorological Agency has distributed relatively high quality seismic data), including the 1978 Miyagi earthquake ( $M_w$ 7.4). The USGS (2012) placed the main shock hypocenter about 129 km east of Sendai (38.297°N, 142.372°E) at a depth of 30 km (USGS 2012). The rupture length (along strike) extended for

---

<sup>a)</sup> University of California, Los Angeles, CA, [jstewart@seas.ucla.edu](mailto:jstewart@seas.ucla.edu)

<sup>b)</sup> Tokyo Institute of Technology, Yokohama, Japan

<sup>c)</sup> US Geological Survey, Pasadena, CA

<sup>d)</sup> PEER Center, University of California, Berkeley, CA

<sup>e)</sup> EQECAT, Inc., Beaverton, OR

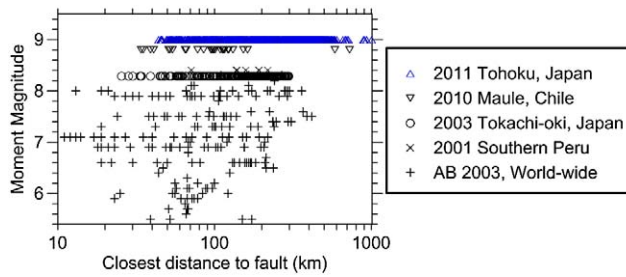


**Figure 1.** Distribution of strong motion data for interface subduction zone earthquakes. Data taken from electronic supplement to [Atkinson and Boore \(2003\)](#) for data prior to 2001, [Rodriguez-Marek et al. \(2010\)](#) for the 2001 Southern Peru earthquake, [Zhao \(2011\)](#) for the 2003 Tokachi-oki earthquake, and [Boroschek et al. \(2012\)](#) for the Maule earthquake.

approximately 480 km, from the north end of Honshu Island to Tokyo Bay in the south, and had a down-dip width of approximately 180 km. The event produced a destructive tsunami, devastating coastal areas including catastrophic damage at the Fukushima nuclear power plant (e.g., [Mori et al. 2013](#)), extensive ground failure from liquefaction and slope instability (e.g., [Cox et al. 2013](#)), but only modest shaking-related damage (e.g., [Okazaki et al. 2013](#), [Kawashima and Buckle 2013](#)).

The Tohoku earthquake is the largest magnitude event to have produced strong motion recordings. Figure 1 shows the strong motion data distribution for worldwide subduction zone interface earthquakes through 2011. The data shown in Figure 1 are from the data set used by [Atkinson and Boore \(2003\)](#), supplemented with the more recent events listed in the legend and caption. The general characteristics of the ground motions from this major event have been described previously by [Furumura et al. \(2011\)](#), [Skarlatoudis and Papazachos \(2012\)](#), and [Midorikawa et al. \(2012\)](#). In the present work, we extend the previous studies by performing more quantitative residuals analysis to investigate event terms, distance attenuation trends, and site effects.

In this article, we begin by describing the geologic and tectonic setting, the seismic sequence, and alternate finite-fault representations of the source from the literature. We select a finite-fault model for use in site-to-source distance calculations. We describe the ground motion database including the record processing procedures that were applied and the evaluation of site conditions from available data resources. We then compare observed spectral accelerations to predictions from four ground motion prediction equations (GMPEs), three of which are international models for subduction zone earthquakes, and one of which is Japan-specific. We formally examine issues related to magnitude-scaling, distance-scaling, site effects, and within-event data dispersion. These results will be directly applicable to the development of next-generation GMPEs for interface subduction zone earthquakes. Analyses of this type have not been performed previously on the Tohoku data set, although where related prior work has been performed (e.g., on the distance attenuation issue), we compare our results to those described previously.

## SETTING AND SOURCE DESCRIPTION

### REGIONAL GEOLOGY

Figure 2 depicts surface geological conditions in the Tohoku region, as well as the Kanto region to the south, which includes Tokyo. Starting from the north end of the earthquake region in the Iwate Prefecture, Figure 2 shows the Kitakami Mountains along the Ria coast, which are composed of Paleozoic-Mesozoic sedimentary rocks, accretionary complexes, and Cretaceous felsic plutonic rocks ([Geospatial Information Authority of Japan 1997](#)). As is typical of island arc systems, behind (west of) the coastal range is a sedimentary depression, which is bounded to the west by the igneous (volcanic) Ou Mountain Range that forms the central backbone of northern Honshu. The Ou range is composed of volcanic and sedimentary rocks from the Late Oligocene and deposits from Quaternary volcanoes, and extends as far south as the Kanto Plain. In northern Honshu, the Ou range is the volcanic front that forms the boundary between the forearc and backarc regions, as discussed below.

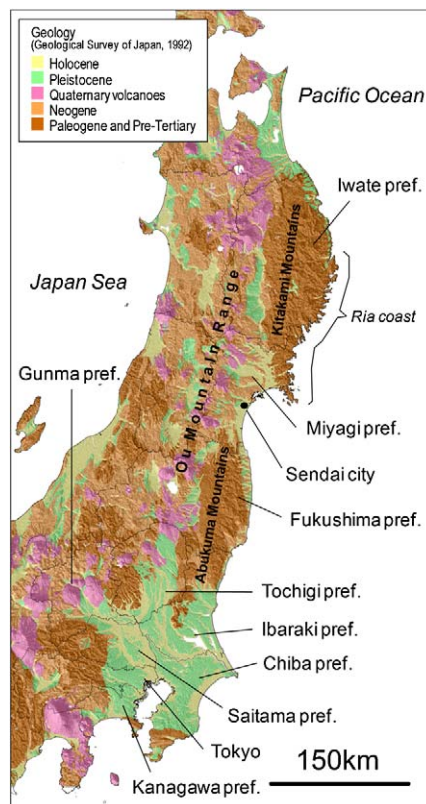


**Figure 2.** Generalized geological map with shaded relief of topography in Tohoku and Kanto regions of Japan. Source: [Geological Survey of Japan \(1992\)](#).

The Sendai Plain occurs at the southwest end of the Kitakami Mountains in the Miyagi Prefecture. The Sendai Plain is comprised of Holocene sediments and is bounded to the west by the Ou Mountain Range and to the south by the coastal Abukuma Mountains. The Abukuma Mountains are similar in composition to the Kitakami Mountains to the north, and as with the northern range, are bounded to the west by a sedimentary depression before reaching the Ou range.

At the south end of the earthquake region is the Kanto Plain, which includes the prefectures of Gunma, Tochigi, Ibaraki, Saitama, Chiba, Kanagawa, and Tokyo. The Kanto Plain is underlain by a large-scale Quaternary sedimentary basin having Holocene sediments in coastal areas and along major rivers to a maximum depth of about 50 m to 100 m. The depth of the sedimentary basin to the Pre-tertiary bedrock reaches approximately 3–4 km.

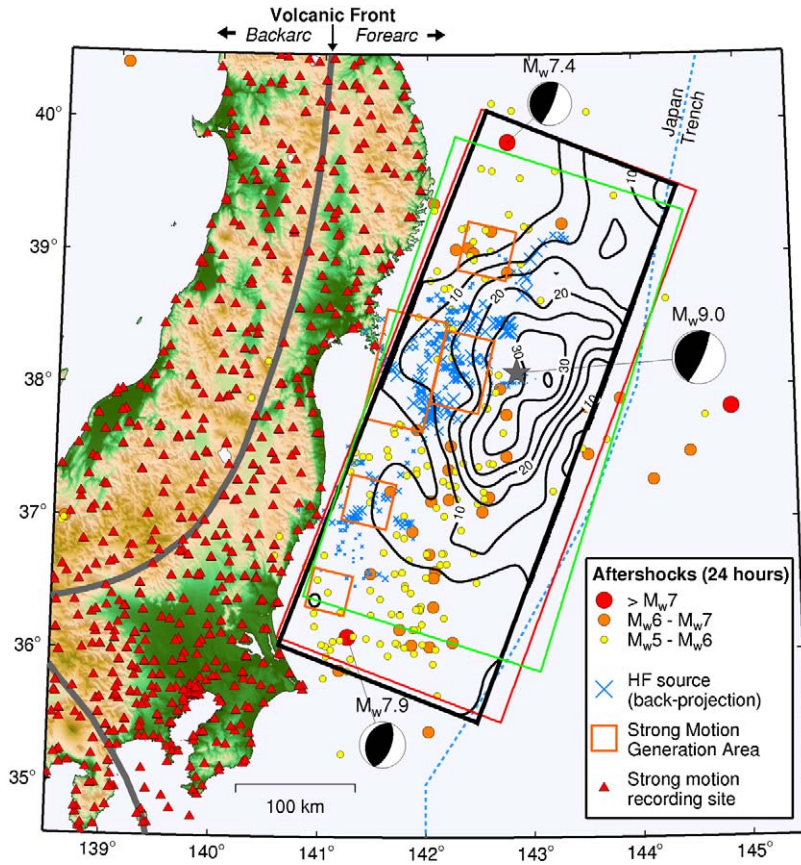
## SEISMIC SEQUENCE

Figure 3 shows the epicenters of the 2011 Tohoku earthquake and its major ( $M_w > 5$ ) aftershocks in the initial 24 hours. Additional information on fault dimensions, slip, and zones of high-frequency energy release are also shown, which are described in subsequent sections. Moment tensor solutions for the main shock and two large aftershocks (from JMA 2012) are also shown. The main shock moment tensor solution has a JMA seismic moment of  $4.22 \times 10^{22} \text{ N} \cdot \text{m}$  ( $4.5 \times 10^{22} \text{ N} \cdot \text{m}$  from the USGS), a hypocentral depth from JMA of 24 km (30 km from the USGS), and a moment magnitude of  $M_w = 9.0$  (from both JMA and the USGS). The moment tensor solutions indicate reverse faulting consistent with a megathrust earthquake. Most of the aftershocks are distributed within the boundaries of the finite-fault model shown in Figure 3, which is roughly 480 km along-strike by 180 km wide down-dip.

Figure 3 also shows a portion of the volcanic front near the study region in Japan. The volcanic front was defined by connecting the locations of major volcanic mountains, and is useful for delineating forearc and backarc regions. Variations in ground motion attenuation in the two regions are discussed subsequently in this article.

## FINITE FAULT MODEL

Models of the rupture process for the Tohoku-oki main shock have been generated from a variety of data sources including geodetic, teleseismic, strong motion, and tsunami. Models generated from joint inversions of multiple data sets are presented by Ammon et al. (2011), Koketsu et al. (2011), Lee et al. (2011), Shao and Ji (2011), Simons et al. (2011), Yokota et al. (2011), and Wei et al. (2012). Simons et al. (2011) was among the first studies to identify the dual nature of the rupture process. In general, the shallow portion of the rupture (up-dip of the hypocenter) was characterized by large ( $>50 \text{ m}$ ) and relatively slow fault displacement, which created the devastating tsunami and generated most of the long-period ( $T > 20 \text{ s}$ ) seismic radiation. Deeper portions of the rupture had relatively low slip, but the slip occurred more quickly than on the shallow fault and resulted in the generation of significant shorter period ( $T < 20 \text{ s}$ ) seismic radiation. Additionally, since the deeper portion of the fault is much closer to Honshu, the strong ground shaking response on-shore was primarily controlled by the deeper rupture (Wei et al. 2012).



**Figure 3.** Map view showing surface projections of the three trimmed fault models (Yokota = black, Shao = green, Wei = red) along with the strong motion generation areas of Kurahashi and Irikura (2011; orange rectangles) and the high-frequency back-projection source locations of Meng et al. (2011; blue crosses). Contours indicate slip (m) for the Yokota rupture model. Colored circles show aftershocks within the first 24 hours following the main shock. Dashed blue line indicates location of Japan Trench and the gray star is the JMA epicenter of the main shock. The red triangles denote the locations of some of the strong motion recording sites considered in our analysis (additional stations were considered beyond the limits of the map).

Studies utilizing multiple data sets in their inversions highlight the importance of considering data spanning a broad frequency range. For example, Koketsu et al. (2011) demonstrate that inversions considering only strong motion data only recover slip on relatively deep portions of the fault, whereas inversions using only geodetic or tsunami data only recover slip on shallow portions of the fault. Combining multiple data sets in the inversion allows the recovery of both the large shallow slip and the relatively smaller displacement, but more seismically energetic, deep slip.

Accordingly, we restricted our analysis to models derived from multiple data sets, where one of the data sources includes strong ground motion data. In the present study, we have considered the models of [Shao and Ji \(2011\)](#), [Yokota et al. \(2011\)](#) and [Wei et al. \(2012\)](#). Slip distribution plots of the three models as projected in plan view are shown in the electronic supplement materials (Figure ES1), while Figure 3 shows slip contours for the [Yokota et al. \(2011\)](#) model. As with all slip model inversions, the resolution of smaller slip values has more uncertainty because larger slip patches dominate the solution. Since the maximum slip in these models is extremely large, ranging from 35 m to 63 m, we have chosen to truncate the slip at a minimum value of 3 m (in Figure ES1, open circles indicate subfaults with slip  $\leq 3$  m). The bounding rectangles shown in Figure ES1 and Figure 3 represent the fault surfaces of these models after trimming rows and columns in which slip on all subfaults is under 3 m, although no trimming was needed for the [Yokota et al. \(2011\)](#) model. The general patterns of slip in the three models are similar, being dominated by large slip on shallow portions of the fault.

Figure 3 shows that the two trimmed models and the [Yokota et al. \(2011\)](#) model are fairly similar, with the main differences being the somewhat shorter eastward (up-dip) extent of the [Yokota et al. \(2011\)](#) model and the shorter north-south (along-strike) extent of the [Shao and Ji \(2011\)](#) model. Also shown in Figure 3 are strong motion generation areas (SMGAs) presented by [Kurahashi and Irikura \(2011\)](#) and the high-frequency (0.5 Hz to 1 Hz) radiation areas evaluated from back-projection of teleseismic array observations by [Meng et al. \(2011\)](#). While these later studies do not provide resolution of the entire fault rupture process, they indicate regions where strong high-frequency energy was emitted and support the inclusion of relatively deep low-slip regions in the trimmed fault models.

Figure 4 plots cross sections of the three trimmed fault models as a function of distance perpendicular to strike, measured from the trench axis. The [Wei et al. \(2012\)](#) model uses a single fault plane, whereas [Shao and Ji \(2011\)](#) and [Yokota et al. \(2011\)](#) use three planes with fault dip increasing with depth. Also shown in Figure 4 is the subducting plate interface given by [Miura et al. \(2005\)](#). The single fault plane of [Wei et al. \(2012\)](#) is only able to closely match the plate interface in the middle portion of the fault. The [Shao and Ji \(2011\)](#) model is

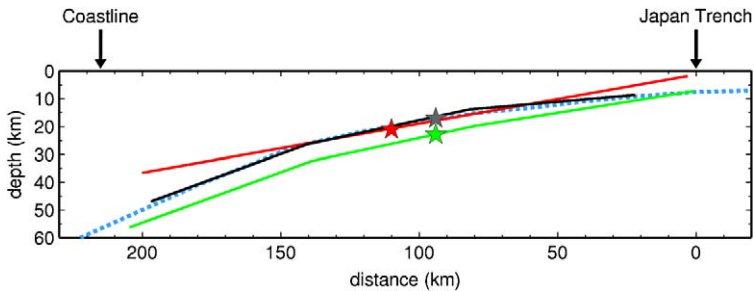


**Figure 4.** Depth cross section perpendicular to fault strike through the main shock hypocenter showing the geometry of the three trimmed fault models (Yokota = black, Shao = green, Wei = red). The colored stars indicate the hypocenter used for each model. Dashed blue line indicates the subducting plate interface from [Miura et al. \(2005\)](#). Locations of Japan Trench and coastline are also indicated.



**Table 1.** [Yokota et al. \(2011\)](#) fault plane segments

Top center <sup>1</sup> longitude	Top center <sup>1</sup> latitude	Strike (deg)	Dip (deg)	depth to top center <sup>1</sup> (km)	Along-strike length (km)	Down-dip width (km)
143.4464	37.4835	200	5	8.65	480	60
142.8276	37.6816	200	12	13.9	480	60
142.2021	37.8775	200	20	26.4	480	60

<sup>1</sup>Top center is the location of the midway point along the upper edge of each fault plane segment.

generally about 5 km to 8 km deeper than the [Miura et al. \(2005\)](#) plate interface, possibly due to their use of the JMA epicenter with a depth of 23 km. [Wei et al. \(2012\)](#) use the hypocenter determined by [Chu et al. \(2011\)](#), which is about 15 km west of the JMA epicenter and has a depth of 21 km. [Chu et al. \(2011\)](#) discuss the importance of hypocenter specification and its tradeoffs with fault geometry and its impact on the resolution of slip distribution for this earthquake. The [Yokota et al. \(2011\)](#) model used the JMA epicenter with a depth of 17 km and their fault geometry provides the closest match to the inferred plate interface.

Based on the above assessments, we have chosen to use the [Yokota et al. \(2011\)](#) fault representation for our distance measurements in the current study. Table 1 gives the locations and dimensions of the [Yokota et al. \(2011\)](#) fault plane segments.

## GROUND MOTION DATABASE

### GROUND MOTION NETWORKS

As described by [Midorikawa et al. \(2012\)](#), research ground motion networks that recorded the Tohoku-oki main shock include the K-NET and KiK-net maintained by the National Research Institute for Earth Science and Disaster Prevention (NIED), PARI-net operated by the Port and Airport Research Institute, and BRI-net operated by the Building Research Institute. Additional networks used for disaster management include the JMA-net operated by the Japan Meteorological Agency, various prefectures networks, and an MLIT network operated by the Ministry of Land, Infrastructure, and Transport.

In the present study, we utilized available data from the K-NET, KiK-net, PARI-net, and JMA-net arrays. The available data were reviewed to identify through visual inspection recordings for which all three components demonstrated a clear onset of shaking, so as to exclude from the data set records that may have had a P-trigger. This process yielded 1,238 triaxial accelerographs, most of which have locations shown in Figure 3. Further information on ground motion networks in Japan and recorded data from the Tohoku-oki main shock are provided by [Midorikawa et al. \(2012\)](#).

### DATA PROCESSING

A total of 1,238 three-component, uncorrected digital accelerograms were selected as described above. Sponsored by the Pacific Earthquake Engineering Research (PEER) center, those motions were processed by Pacific Engineering and Analysis following PEER/NGA

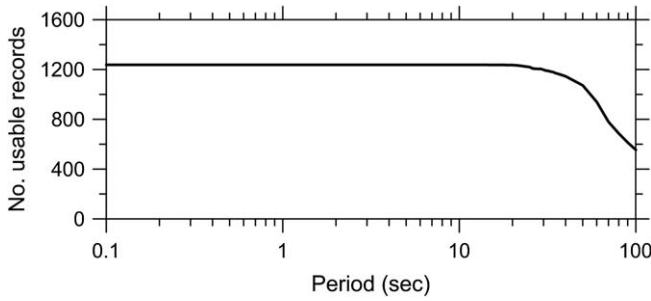


**Figure 5.** Number of usable two-component horizontal records as function of spectral period for the data set considered in this study.

protocols (Darragh et al. 2004, Chiou et al. 2008), which include selection of record-specific corner frequencies to optimize the usable frequency range. For KiK-net sites, only data from the ground surface stations are considered. The most important filter applied to the data is the low-cut filter, which removes low-frequency noise effects. We take the minimum usable frequency as  $1.25 \times f_{HP}$ , where  $f_{HP}$  is the high-pass (equivalent to low-cut) corner frequency used in the processing. Using the filtered records, we computed the intensity measures of peak acceleration (PGA), peak velocity (PGV), and pseudo-acceleration response spectra at a range of periods between 0.01 sec and 10.0 sec. Figure 5 presents the number of usable recordings as a function of period. A usable recording for period  $T$  is defined as having both horizontal components with  $T < 1/(1.25f_{HP})$ . The data set is seen to fall off for periods beyond about 20 sec to 30 sec.

## SITE CONDITIONS

The NIED website contains shear- and compression-wave velocity profiles for each of the K-NET and KiK-net sites except for five ocean-bottom sites. KiK-net profiles are always deeper than 30 m, whereas K-NET profiles are always 20 m or shallower. The measured shear wave velocity profiles were used to compute  $V_{S30}$  as follows:

1. When profile depth ( $z_p$ ) is 30 m or greater (KiK-net sites), the  $V_s$  profile is used to compute  $V_{S30}$  as the ratio of 30 m to the shear wave travel time above a depth of 30 m.
2. When  $z_p < 30$  m, compute  $V_{S_z}$  as the ratio of  $z_p$  to shear wave travel time from  $z_p$  to the ground surface.
3. When  $z_p = 20$  m, compute  $V_{S30}$  from  $V_{S_z}$  and  $z_p$  using the correlation relationships originally developed for California by Boore (2004). When  $z_p \leq 10$  m, compute  $V_{S30}$  from  $V_{S_z}$  and  $z_p$  using the correlation relationships developed from KiK-net data by Boore et al. (2011). For intermediate depths of  $10 < z_p < 20$  m, interpolate between the above values.

The rationale behind Step (3) above is that shallow-depth K-NET profiles likely encountered firm geologic materials causing borehole drilling to stop. Firm geologic conditions are



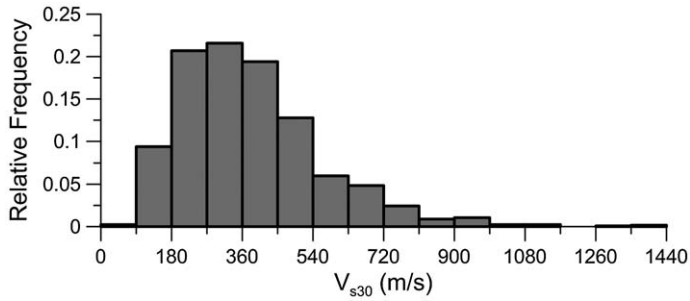


**Figure 6.** Histogram of  $V_{s30}$  values in data set.

also common for KiK-net sites. On the other hand, 20 m K-NET profiles are likely deeper sediments similar to the conditions prevalent in California. A histogram of  $V_{s30}$  values in the data set is shown in Figure 6. No velocity profiles are available for the five ocean-bottom sites and  $V_{s30}$  was assumed as 180 m/s for the present study.

For sites without velocity profiles, which includes all of the JMA-net and 9 of 20 PARI-net sites, we estimate  $V_{s30}$  using a proxy-based method described by Matsuoka et al. (2006). This method uses geomorphic and geologic conditions mapped across Japan (Wakamatsu and Matsuoka 2008) that are correlated by category to  $V_{s30}$ .

## DISTANCE CALCULATION

We computed distances from each utilized recording station to the finite-fault rupture model shown in Figure 3 (and Table 1). The distance parameters that were computed are rupture distance ( $R_{rup}$ ) and Joyner-Boore distance ( $R_{jb}$ ), which is the closest distance to the surface projection of the rupture surface.

## COMPARISONS TO GMPEs

In this section, we compare the Tohoku-oki earthquake main shock data described in the previous section to several GMPEs using an approach, originally presented by Scasserra et al. (2009), in which specific attributes of the GMPE are examined relative to the data. In particular, we investigate the implications of the data for magnitude scaling, distance scaling, intra-event dispersion, and site effects. An alternative approach was presented by Scherbaum et al. (2004), in which overall goodness of fit of data to a model is computed by comparing normalized residuals to the standard normal variate. The selected approach was used because we seek the aforementioned physical insights provided by the ground motion data.

## APPLICABLE MODELS

We utilize ground motion prediction equations (GMPEs) for interface subduction zone earthquakes by Atkinson and Boore (2003, 2008), Abrahamson et al. (2013), and Zhao et al. (2006), which we refer to subsequently as AB 2003, AEA 2013, and ZEA 2006, respectively. The first and third of these GMPEs were used to predict subduction zone ground motions in the USGS seismic hazard maps (Petersen et al. 2008). The AEA 2013 model has been

identified for use in subsequent versions of the USGS maps. We also consider a Japan-specific model by [Si and Midorikawa \(2000\)](#) that utilizes Japanese data from crustal, inter-plate, and intra-plate events. That model, which applies to PGA and PGV only, was selected due to its widespread usage in Japan, and it is denoted as SM 2000.

AB 2003 is based on worldwide subduction zone data and includes models specific to various regions of the world, including South America and Japan. The generic, non-regional version of the model is used here and the event terms are subsequently used to check the AB 2003 regional correction for Japan. We recognize that Atkinson and Macias (2009) have developed a subsequent GMPE for subduction regions, derived in part from simulations of large subduction earthquakes, which they recommend over AB 2003. The original AB 2003 model was selected due to its usage in numerous engineering applications ([Petersen et al. 2008](#), [Stewart et al. 2013](#)). The largest magnitude in the AB data set is 8.3 and the largest well-recorded event is 8.0. ZEA 2006 and SM 2000 utilize data from worldwide crustal events, and they use Japanese data from multiple source types including interface and intra-slab subduction zone earthquakes. The AB and ZEA models apply to the geometric mean of the two horizontal components, whereas SM 2000 applies to the larger of two horizontal components. The developers of the AB, SM, and ZEA models each indicated their equations as applicable to an upper bound magnitude of 8.3. The AEA model is considered to be applicable to magnitude 9.0.

## MAGNITUDE SCALING OF SPECTRAL ORDINATES

A key issue in ground motion prediction for interface subduction zone earthquakes is the functional form used for magnitude scaling. Many models produce essentially linear scaling of the logarithm of ground motion with magnitude (e.g., SM model in Figure 7 and a linear form of ZEA that is not used here), whereas others apply higher order terms that produce saturation of ground motion with increasing magnitude (e.g., AB 2003 and AEA 2013 models, as well as quadratic form of ZEA 2006 model in Figure 7). The SM 2000 model predictions shown in Figure 7 and elsewhere have been divided by 1.1 to correct from largest horizontal component to the geometric mean, based on the recommendations of [Beyer and Bommer \(2006\)](#).

In Figure 7, we plot ground motion intensity measures (IMs) at several spectral periods versus magnitude. The data are from AB 2003 (database available through an electronic supplement), the 2001 Southern Peru earthquake ([Rodriguez-Marek et al. 2010](#)), the Maule, Chile, earthquake ([Boroschek et al. 2012](#)), and Tohoku-oki earthquake. The data plotted have rupture distances between 70 km and 150 km and include all site conditions. The GMPE medians are for a distance of 100 km and an average site condition corresponding to  $V_{S30} = 300$  m/s. The data for the Maule and Tohoku events appears to support saturation of ground motions at large magnitudes for the IMs considered, especially for high-frequency IMs.

## DISTANCE SCALING AND RESIDUALS ANALYSIS

Figure 8a shows RotD50 values (i.e., median of single-azimuthal ground motions; [Boore, 2010](#)) for PGA, 0.1s, 1.0 s, and 3.0 s pseudo spectral accelerations (PSa) at 5% damping versus rupture distance. Data are shown for the following bins of  $V_{S30}$ : <200 m/s,

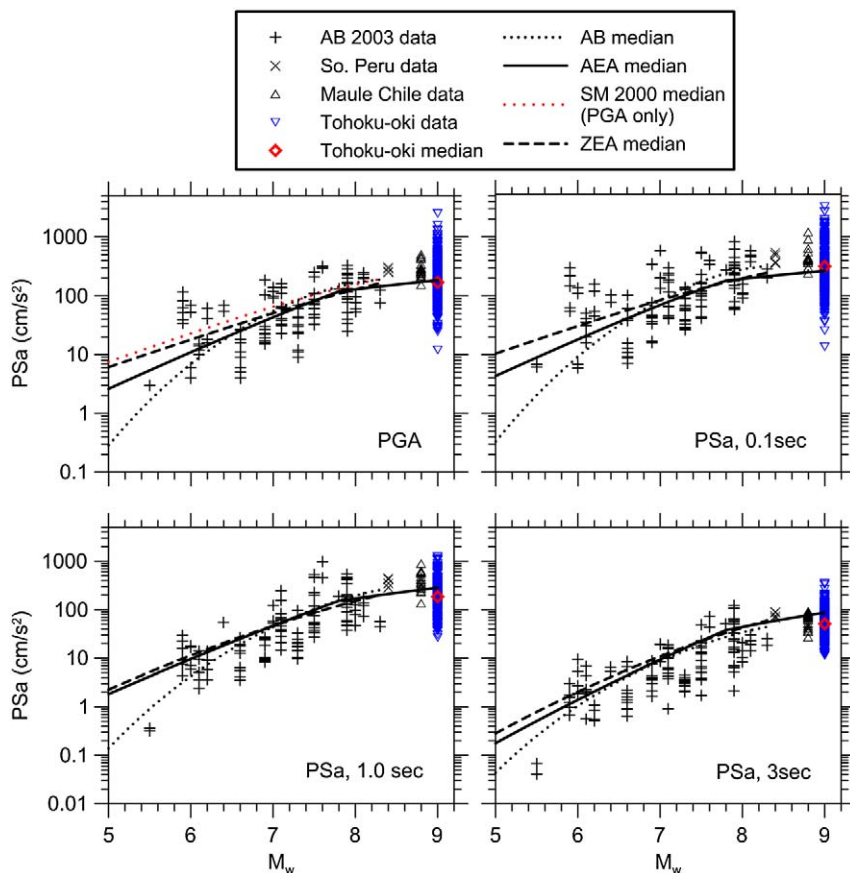


**Figure 7.** Scaling of spectral ordinates and PGA with magnitude from AB 2003 data set as well as Southern Peru, Maule (Chile) and Tohoku-oki earthquake data for distances between 70 km and 150 km. Median predictions from three GMPEs shown, which apply for reference soil conditions (approximate  $V_{S30} = 300$  m/s) and distance of 100 km.

200–400 m/s, 400–760 m/s, and  $> 760$  m/s. Also shown in Figure 8a are means and medians  $\pm$  one within-event standard deviation ( $\phi_m$ ) for the ZEA 2006 GMPE and medians for AB 2003 (without regional correction for Japan), AEA 2013 (for forearc and backarc regions) and SM 2000 (PGA only). The GMPEs are plotted for site categories corresponding to a reference condition of  $V_{S30} = 300$  m/s. All of the GMPEs except AEA 2013 were extrapolated beyond the reported maximum usable magnitude for the present application.

Several significant trends are evident from Figure 8a. First, we see that the ZEA 2006, SM 2000, and AEA 2013 GMPEs have faster distance attenuation rates than AB 2003, and in addition, the data consistently attenuate faster with distance than predicted by AB 2003. ZEA 2006 appears to capture the distance attenuation rate at the two longer considered periods (1.0 and 3.0 sec), but it cannot capture the relatively fast attenuation of high-frequency parameters (0.1 sec PSa and PGA) beyond about 100 km. The SM 2000 trend for PGA is nearly identical

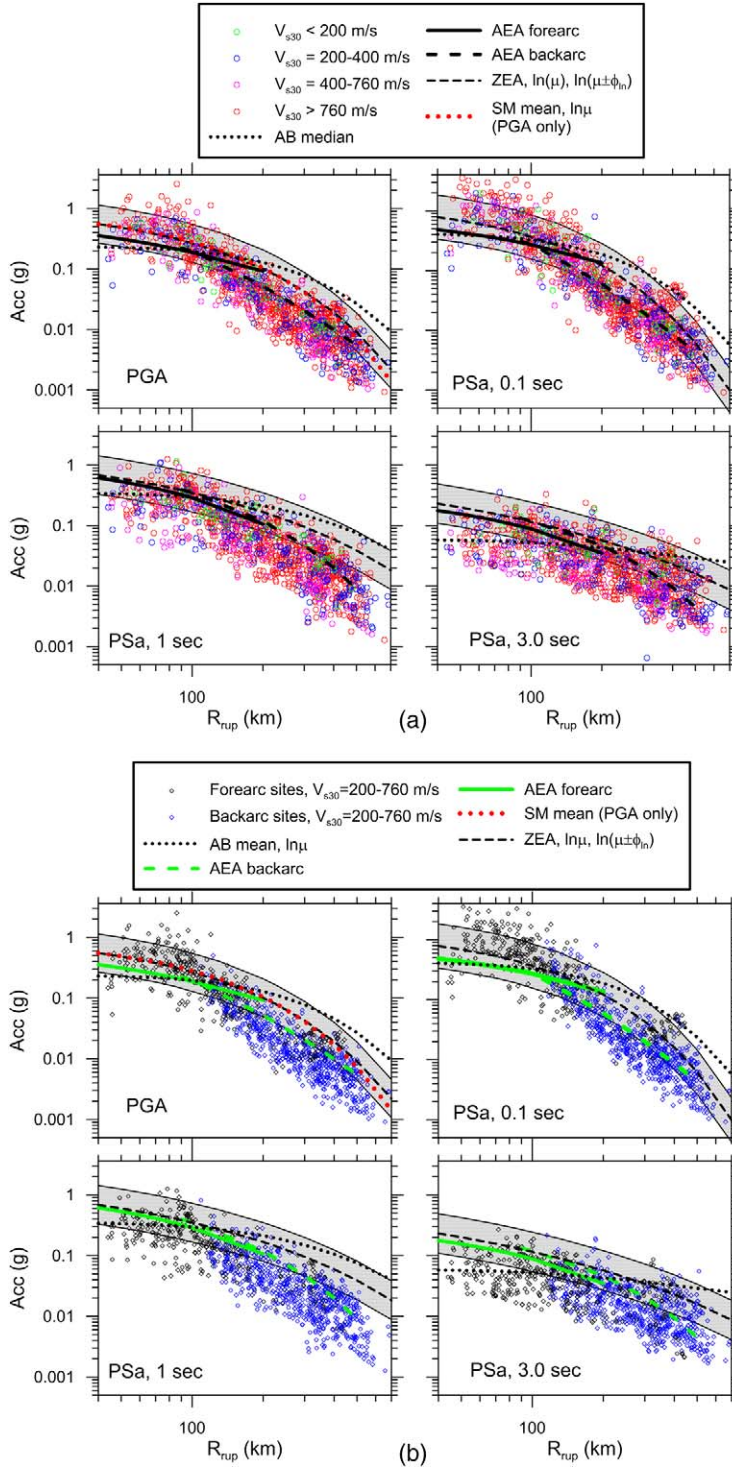


**Figure 8.** (a) Attenuation of PGA and spectral accelerations with distance and comparison to GMPEs for reference condition equivalent to  $V_{s30} = 300$  m/s. For ZEA 2006 both the mean ( $\ln \mu$ ) and mean  $\pm$  one standard deviation ( $\ln(\mu \pm \phi_{ln})$ ) are shown, whereas for AB 2003, AEA 2013, and SM 2000 only means are shown. The data are plotted as geometric means. ZEA 2006 applies to the geometric mean. AB 2003 applies to random component and no correction to the AB 2003 median has been applied. The SM 2000 median is divided by 1.1 to adjust from larger component to geometric mean per the recommendations of [Beyer and Bommer \(2006\)](#). (b) Same as Figure 8a except that data sorted into forearc and backarc sites and only data having  $V_{s30} = 200 - 760$  m/s are shown.

to that of ZEA 2006. Average site effects are also evident from the data in Figure 8; soil sites (green and blue dots) are clearly higher on average than rock sites (purple and red dots) at the longer periods, but this trend does not hold for PGA or 0.1 sec PSa. Site effects are analyzed more formally in the following section.

Figure 8b shows the data from Figure 8a segregated into forearc and backarc regions according to the boundary in Figure 3. Data are shown only for intermediate site classes having  $V_{S30} = 200 - 760$  m/s. The break in slope that occurs in the high-frequency data near  $R_{rup} = 100 - 200$  km is seen to be the consequence of a transition from predominantly forearc to backarc sites. The relatively rapid attenuation in backarc regions is thought to result from increased anelastic attenuation (Ghofrani and Atkinson 2011). AEA 2012 is the only GMPE that incorporates the slope break associated with the forearc to backarc transition, and the backarc model does provide an improved fit, especially at short periods.

To more accurately evaluate the performance of the GMPEs, including corrections for site effects, we calculate total residuals (including inter- and intra-event components; see, for example, Scasserra et al. 2009 for further explanation of the methodology) for each data point considering the appropriate source distance and site condition as follows:

$$R_i = \ln(IM_i)_{rec} - (\mu_i)_{GMPE} \quad (1)$$

where  $(IM_i)_{rec}$  = value of ground motion intensity measure from recording  $i$  and  $(\mu_i)_{GMPE}$  = mean value of that same IM (in natural log units) from the GMPEs. Residuals in forearc and backarc regions are plotted versus distance in Figure 9 along with running means for distance bins. In forearc regions, the AEA 2013 residuals show a generally flat trend for distances up to approximately 150–200 km. At high frequencies, forearc residuals for all three GMPEs trend downward beyond approximately 150–200 km and then trend sharply upward beyond approximately 250 km. The sites producing the upward trend are principally on the southeast (forearc) side of Hokkaido. We do not know what feature of the crustal structure in this region might be responsible for this trend, although high  $Q$  (low crustal damping) has been noted in this region by Hashida (1987). The downward trends of high-frequency forearc residuals for models AB and ZEA extend to close distances (approximately 50 km). At periods of 1.0 and 3.0 sec, the forearc residual trends are quite different among the three models, with AB trending strongly downward, AEA 2013 trending upward, and ZEA 2006 being relatively flat.

The backarc region, which begins at approximately 110 km, has high-frequency residuals that trend downward to at least 300 km, especially for AB 2003 and ZEA 2006. This trend flattens or reverses beyond approximately 200 km (for AEA 2012) and 300 km (for AB 2003 and ZEA 2006). At longer periods, the backarc residuals follow generally similar trends to those in the forearc region, which is expected because the different anelastic attenuation of backarc regions has less effect for long-period ground motion components. The general trends we have noted regarding the misfit of models to data at large distance is consistent with observations from prior studies (e.g., Furumura et al. 2011, Skarlatoudis and Papazachos 2012, and Midorikawa et al. 2012). The relatively strong distance attenuation in backarc regions has been noted previously by Ghofrani and Atkinson (2011) and Skarlatoudis and Papazachos (2012).



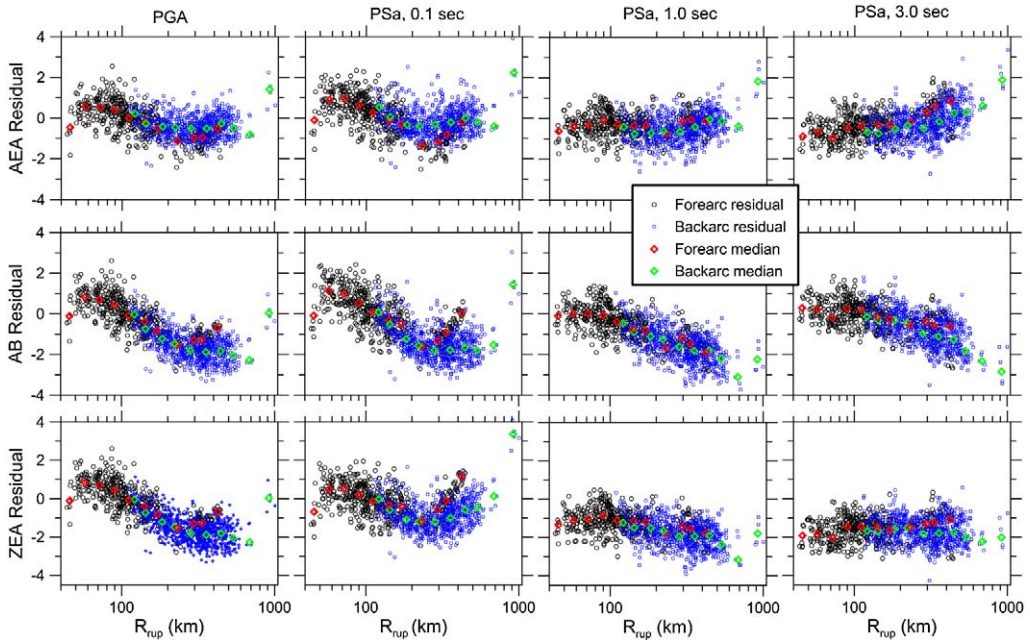


**Figure 9.** Total residuals of Tohoku-oki recordings within forearc and backarc regions relative to AB 2003, AEA 2012, and ZEA 2006 GMPEs along with mean residuals within distance bins.

As shown in Figure 9, in most cases, the data clouds are not centered at zero ordinate, indicating systematic misfits of the GMPEs relative to the data. Since the event is very well recorded, this bias is practically equivalent to an event term as would be calculated from a mixed-effects regression (e.g., [Abrahamson and Youngs 1992](#)). **Non-zero event terms ( $\eta$ ) are typical;** what is of interest is to see if the Tohoku-oki event terms are consistent with event-to-event scatter (represented by event term dispersion  $\tau$ ) and regional trends of GMPE bias as observed from previous earthquakes. Figure 10 shows event terms, calculated as the median residual within 100 km, for the AB 2003, AEA 2013, and ZEA 2006 GMPEs as a function of spectral period along with the  $\pm\tau$  model (inter-event standard deviation) from AB 2003. We only use residuals within 100 km because of the aforementioned distance attenuation misfits, which should not be mapped into event terms. **The event terms peak at about 0.1 sec and decrease at longer periods. The AB 2003 event terms follow closely the Japan region bias reported by AB 2003 (their Table 3),** indicating that the misfit of the Tohoku-oki data relative to the AB 2003 model is consistent with previous data from Japan used in the development of the AB 2003 GMPE.

Event-specific within-event standard deviations in natural log units (denoted as  $\phi_{ln}$ ) can be calculated as the standard deviation of residuals from Equation 1. We compute this dispersion using residuals for all distances. Because the GMPE and data attenuation rates are significantly different, especially at short periods, the  $\phi_{ln}$  values computed from data are higher than those from the GMPEs. Figure 11 shows that standard deviations for AEA 2013 and ZEA 2006 are substantially lower than those from AB 2003 at short periods,



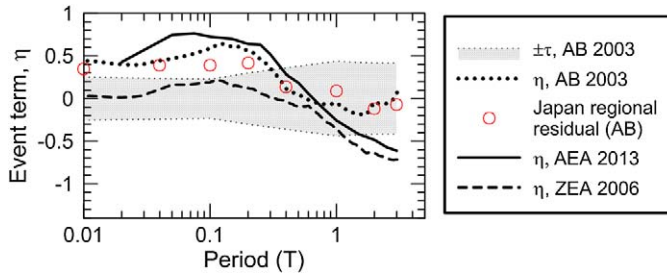


**Figure 10.** Estimated event terms of Tohoku-oki main shock relative to the AB 2003, AEA 2013, and ZEA 2006 GMPEs. Also shown is the AB inter-event standard deviation ( $\tau$ ) and the AB regional model bias for Japan (red circles). Estimated event terms were computed using data with  $R_{rup} < 100$  km.

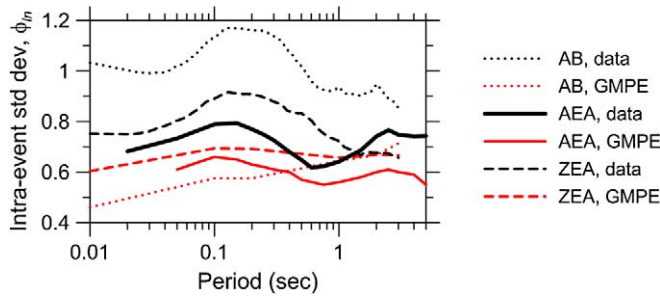


**Figure 11.** Intra-event standard deviation for Tohoku-oki earthquake data as compared to the AB 2003, AEA 2012, and ZEA 2006 intra-event standard deviations,  $\phi_{in}$ . Dispersion computed using data over all distances.

which is due to more accurate distance attenuation. At long periods, dispersion levels for AEA 2012 and ZEA 2006 residuals fall to levels near those from the GMPEs.

## SITE EFFECTS

In this section, we present a preliminary evaluation of **site amplification**, specifically in reference to the scaling of ground motions with  $V_{S30}$ . As of this writing, we have not formally investigated higher-order effects such as nonlinearity in site response, which will be the subject of future work.

To evaluate site amplification, we utilize a non-reference site approach in which residuals are calculated between data and a GMPE applied for reference rock site conditions as follows:

$$R_i^r = \ln(IM_i)_{rec} - ((\mu_i^r)_{GMPE} + \eta) \quad (2)$$

where  $R_i^r$  indicates the residual of recording  $i$  from a rock GMPE,  $\mu_i^r$  is a rock GMPE mean (in natural log units) for the magnitude and distance corresponding to recording  $i$ , and  $\eta$  is the event term appropriate for the earthquake event and IM. The reference site condition is

taken as reference rock for AB 2003 (their site parameters  $S_C$ ,  $S_D$ , and  $S_E$  are set to zero),  $V_{S30} = 1,100$  m/s for AEA 2013, and hard rock for ZEA 2006 (equivalent to NEHRP site category A).

A meaningful analysis of site effects from the Tohoku data set is complicated by the significant distance attenuation misfits identified in the previous section, which cause large non-zero residuals for reasons unrelated to site response. Accordingly, for the analysis of site effects, we use a subset of the data from forearc sites at rupture distances  $R_{rup} < 200$  km, for which distance attenuation trends are relatively well-matched by the GMPEs. Figure 12 shows the trends of AEA 2013 reference site residuals against  $V_{S30}$  for the intensity measures of PGA and PSa at 0.1 sec, 1.0 sec, and 3.0 sec. A log-linear regression using all data is also shown along with its 95% confidence intervals. Figure 13 shows the slopes of these fit lines (denoted as  $c$ ) for the three models as a function of period, which are seen to be similar. Also shown in Figure 13 for reference purposes are similarly computed slopes applicable to active crustal regions (ACRs), which were mostly from California (Choi and Stewart 2005).

The most important observation from the data trends in Figure 12 is the trend (or lack thereof) of reference site residuals with increasing  $V_{S30}$ . Low-frequency ground motions show a statistically significant trend as indicated by the negative slope of the fit line ( $c < 0$ ), whereas high-frequency ground motions have a nearly zero, or even positive, slope. As shown in Figure 13, these slopes are different from the average for active crustal regions (ACRs) evaluated by Choi and Stewart (2005), which are significantly negative at low and high frequencies. These differences are of considerable practical importance, as it suggests that the scaling of ground motions with  $V_{S30}$  may be region-dependent. Although

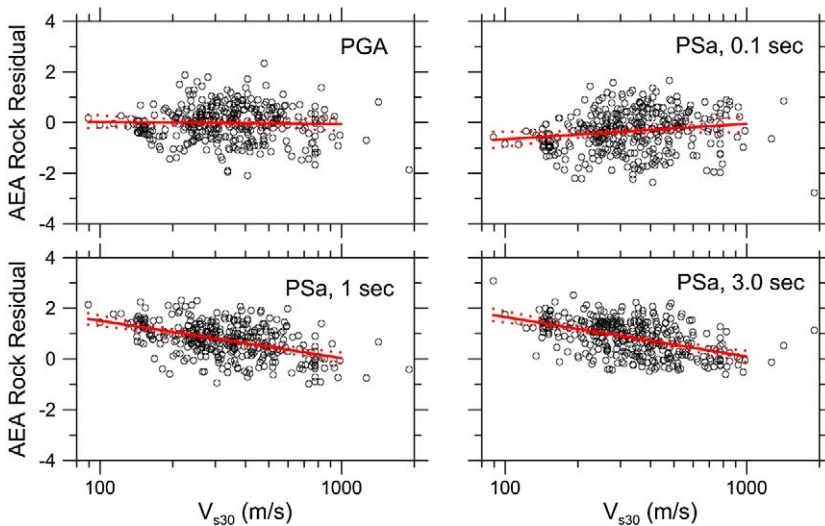


**Figure 12.** Reference rock residuals of Tohoku-oki recordings using AEA 2013 GMPE for rock site conditions. Residuals shown for forearc data with  $R_{rup} < 200$  km along with linear regression fit and confidence intervals.

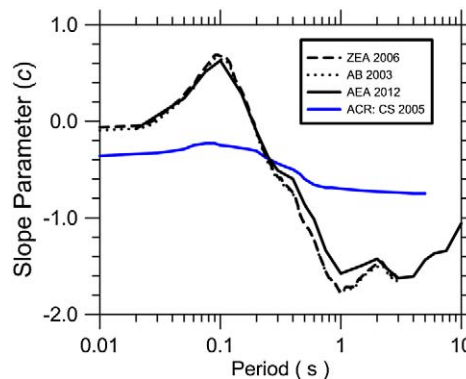


**Figure 13.**  $V_{S30}$ -scaling of reference rock residuals from Tohoku-oki recordings (c parameter) along with comparable values for data from active crustal regions (Choi and Stewart 2005).

unpublished as of this writing, similar findings have been found in the NGA-West 2 project through a similar (i.e., with distance cut-off) examination of an extensive set of ACR data. Regional variations in site response have been observed in previous research, although not (to our knowledge) in the form of regionally variable  $V_{S30}$ -scaling relationships. Atkinson and Casey (2003) computed different site responses using quarter-wavelength theory for Japan and the Pacific Northwest, which explained regional differences in ground motions. Moreover, Oth et al. (2011) and Ghofrani et al. (2013) have observed site response features in Japan, including significant high-frequency amplification, which is seldom encountered in other active regions, such as California.

We note that the data for high-frequency IMs in Figure 12 show principally negative residuals between  $V_{S30} \approx 130$  m/s and 200 m/s, which has been observed previously from Japanese data by the last author (KWC). It is not known whether this trend is sufficiently robust to support the use of a nonlinear  $V_{S30}$ -scaling relationship.

## SUMMARY AND CONCLUSIONS

The Tohoku-oki event is the largest-magnitude earthquake to produce usable recordings. In combination with the data from the 2010 Maule, Chile, earthquake (Boroschek et al. 2012), the data can be used to evaluate magnitude scaling of various ground motion intensity measures (IMs), which has generally been represented with linear or quadratic functions in recent GMPEs for subduction zone interface earthquakes. The data support saturation of the logarithm of IMs with increasing magnitude for the IMs considered, especially at high frequencies, indicating that linear magnitude scaling should not be used for large magnitudes.

The data demonstrate a scaling with distance that is demonstrably faster in backarc than forearc regions for high-frequency IMs. In both forearc and backarc regions, the AEA 2013 model best captures the high-frequency distance attenuation trends. All of the models underpredict the attenuation rate in backarc regions for high-frequency IMs for rupture distances under about 200 km to 300 km. Distance attenuation misfits are mixed among the three models at long periods, being too-fast for AEA 2013, too-slow for AB 2003, and about right for ZEA 2006. The high-frequency distance attenuation trends are different from

those from the Maule event (Boroschek et al. 2012), where distance attenuation rates were slower and were well captured by the AB 2003 model and overpredicted by the ZEA 2006 model.

Using a non-reference site approach, we find that the scaling of site amplification with  $V_{S30}$  is weak to nonexistent for high-frequency ground motions, but strong for low frequencies. Given the well-established and significant scaling of site amplification at low and high frequencies observed elsewhere (principally California), these findings suggest that the  $V_{S30}$  scaling of ground motions may have regional dependence. This is not particularly surprising given that  $V_{S30}$  is a proxy for geologic structure, and since geologic conditions are regionally variable (e.g., Atkinson and Casey 2003), the scaling of ground motion with  $V_{S30}$  can therefore also be expected to be region-dependent. Similar findings (unpublished) are also emerging from analysis of shallow crustal earthquake data in the NGA-West 2 project, indicating that this trend is not confined to this single earthquake.

We evaluate event terms using recordings within rupture distances of 100 km because the problems with distance attenuation become particularly pronounced beyond that distance. Event terms are generally positive (indicating underprediction) for periods less than 0.7 sec to 1.0 sec and peak at about 0.1 sec to 0.2 sec. At periods longer than about 1.0 sec, the AB event terms are nearly zero, whereas AEA 2013 and ZEA 2006 event terms are negative. The AB 2003 event terms follow quite well the regional bias for Japan presented by AB 2003 with their Japan-specific regional correction factor.

Within-event dispersion levels are higher than those from the corresponding GMPEs at high frequencies due to the distance attenuation misfits. The AEA 2013 and ZEA 2006 models have the lowest high-frequency dispersion levels among the three models. AB 2003 residuals have the highest dispersion due to the relatively large distance attenuation misfit. At long periods, dispersion levels for the AEA 2013 and ZEA 2006 residuals fall to levels near those from the corresponding GMPEs.

## ACKNOWLEDGEMENTS

The participation of the first author in reconnaissance activities for this earthquake was supported by the Geotechnical Extreme Events Reconnaissance (GEER) Association, which receives financial support from the National Science Foundation. Partial support from the USGS, through NEHRP funding to PEER, is gratefully acknowledged. We thank Elizabeth Cochran, Paul Spudich, Gail Atkinson, and two anonymous reviewers for their helpful and insightful reviews of this manuscript, which have improved the final product.

## REFERENCES

- Abrahamson, N. A., and Youngs, R. R., 1992. A stable algorithm for regression analyses using the random effects model, *Bull. Seism. Soc. Am.* **82**, 505–510.
- Abrahamson, N. A., Gregor, N., and Addo, K., 2012. BChydro ground motion prediction equations for subduction earthquakes, *Earthquake Spectra*, submitted.
- Ammon, C. J., Lay, T., Kanamori, H., and Cleveland, M., 2011. A rupture model of the 2011 off the Pacific coast of Tohoku Earthquake, *Earth Planets Space* **63**, 693–696.

- Atkinson, G. M., and Boore, D. M., 2003. Empirical ground-motion relations for subduction-zone earthquakes and their application to Cascadia and other regions, *Bull. Seism. Soc. Am.* **93**, 1703–1729.
- Atkinson, G. M., and Boore, D. M., 2008. Erratum to empirical ground-motion relations for subduction zone earthquakes and their application to Cascadia and other regions, *Bull. Seism. Soc. Am.* **98**, 2567–2569.
- Beyer, K., and Bommer, J. J., 2006. Relationships between median values and between aleatory variabilities for different definitions of the horizontal component of motion, *Bull. Seism. Soc. Am.* **96**, 1512–1522.
- Boore, D. M., 2010. Orientation-independent, nongeometric-mean measures of seismic intensity from two horizontal components of motion, *Bull. Seism. Soc. Am.* **100**, 1830–1835.
- Boore, D. M., 2004. Estimating  $V_{S30}$  (or NEHRP site classes) from shallow velocity models (depth < 30 m), *Bull. Seism. Soc. Am.* **94**, 591–597.
- Boore, D. M., Thompson, E. M., and Cadet, H., 2011. Regional correlations of  $V_{S30}$  and velocities averaged over depths less than and greater than 30 m, *Bull. Seism. Soc. Am.* **101**, 3046–3059.
- Boroscchek, R., Contreras, V., Kwak, D. Y., and Stewart, J. P., 2012. Strong ground motion attributes of the 2010  $M_w$  8.8 Maule Chile Earthquake, *Earthquake Spectra* **28**, S19–S38.
- Chiou, B. S.-J., Darragh, R., Dregor, D., and Silva, W. J., 2008. NGA project strong-motion database, *Earthquake Spectra* **24**, 23–44.
- Choi, Y., and Stewart, J. P., 2005. Nonlinear site amplification as function of 30 m shear wave velocity, *Earthquake Spectra* **21**, 1–30.
- Chu, R. S., Wei, S., Helmberger, D., Kanamori, H., Zhan, Z. W., and Zhu, L. P., 2011. Beginning of the great  $M_w = 9.0$  Tohoku-Oki earthquake, *Earth and Planetary Sciences Letters* **308**, 277–283.
- Cox, B. R., Boulanger, R. W., Tokimatsu, K., Wood, C., Abe, A., Ashford, S. A., Donahue, J., Ishihara, K., Kayen, R. E., Katsumata, K., Kishida, T., Kokusho, T., Mason, H. B., Moss, R. E. S., Stewart, J. P., Tohyama, K., and Zekkos, D., 2013. Liquefaction at strong motion stations in Urayasu City during the 2011 Tohoku-oki earthquake, *Earthquake Spectra* **29**, S55–S80.
- Darragh, R., Silva, W. J., and Gregor, N., 2004. Strong motion record processing for the PEER center, *Proc. Workshop on Strong Motion Record Processing*, Richmond, CA, 26–27 May 2004, available at <http://www.cosmos-eq.org/recordProcessingPapers.html>.
- Furumura, T., Takemura, S., Noguchi, S., Takemoto, T., Maeda, T., Iwai, K., and Pdhy, S., 2011. Strong ground motions from the 2011 off-the Pacific-Coast-of-Tohoku, Japan ( $M_w = 9.0$ ) earthquake obtained from a dense nationwide seismic network, *Landslides* **8**, 333–338.
- Geological Survey of Japan, 1992. Geological Map of Japan, Third Edition, CD-ROM version, 1:1,000,000.
- Geospatial Information Authority of Japan, 1997. *The National Atlas of Japan* (CD-ROM).
- Ghofrani, H., and Atkinson, G. M., 2011. Forearc versus backarc attenuation of earthquake ground motion, *Bull. Seism. Soc. Am.* **101**, 3032–3045.
- Ghofrani, H., Atkinson, G. M., and Goda, K., 2012. Implications of the 2011  $M_w$  9.0 Tohoku Japan earthquake for the treatment of site effects in large earthquakes, *Bull. Earthquake Eng.* **11**, 171–203.
- Hashida, T., 1987. Determination of three-dimensional attenuation structure and source acceleration by inversion of seismic intensity data: Japanese islands, *Bull. Earthquake Research Institute, University of Tokyo*, **62**, 247–287.

- Japan Metrological Agency (JMA), 2012. *Centroid Moment Tensor (CMT) Solutions*, available at <http://www.seisvol.kishou.go.jp/eq/mech/cmt/cmt201103.html> (last accessed March 2012).
- Kawashima, K., and Buckle, I., 2013. Structural performance of bridges in the 2011 Tohoku-oki earthquake, *Earthquake Spectra* **29**, S315–S338.
- Koketsu, K., Yokota, Y., Nishimura, N., Yagi, Y., Miyazaki, S., Satake, K., Fujii, Y., Miyake, H., Sakai, S., Yamanaka, Y., and Okada, T., 2011. A unified source model for the 2011 Tohoku earthquake, *Earth and Planetary Science Letters* **310**, 480–478.
- Kurahashi, S., and Irikura, K., 2011. Source model for generating strong ground motions during the 2011 off the Pacific coast of Tohoku Earthquake, *Earth Planets Space* **63**, 571–576.
- Lee, S. J., Huang, B. S., Ando, M., Chiu, H. C., and Wang, J. H., 2011. Evidence of large scale repeating slip during the 2011 Tohoku-Oki earthquake, *Geophys. Res. Lett.* **38**, No. 19, L19306, doi:10.1029/2011GL049580.
- Matsuoka, M., Wakamatsu, K., Fujimoto, F., and Midorikawa, S., 2006. Average shear-wave velocity mapping using Japan engineering geomorphologic classification map, *Journal of Structural Mechanics and Earthquake Engineering* **23**, 57s–68s.
- Meng, L. S., Inbal, A., and Ampuero, J. P., 2011. A window into the complexity of the dynamic rupture of the 2011 Mw 9 Tohoku-Oki earthquake, *Geophys. Res. Lett.* **38**, L00G07, doi:10.1029/2011GL048118.
- Midorikawa, S., Miura, H., and Atsumi, T., 2012. Strong ground motion during the 2011 Off the Pacific Coast of Tohoku earthquake, *Proc. 9th Int. Conf. on Urban Earthquake Eng. & 4th Asia Conf. on Earthquake Eng.*, 6–8 March 2012, Tokyo Institute of Technology, Tokyo, Japan.
- Miura, S., Takahashi, N., Nakanishi, A., Tsuru, T., Kodaira, S., and Kaneda, Y., 2005. Structural characteristics off Miyagi forearc region, the Japan Trench seismogenic zone, deduced from a wide-angle reflection and refraction study, *Tectonophysics* **407**, 165–188.
- Mori, N., Cox, D. T., Yasuda, T., and Mase, H., 2013. Overview of the 2011 Tohoku earthquake tsunami damage in relation to coastal protection along the Sanriku Coast, *Earthquake Spectra* **29**, S127–S143.
- Okazaki, T., Lignos, D. G., Midorikawa, M., Ricles, J. M., and Love, J., 2013. Damage to steel buildings observed after the 2011 Tohoku-oki earthquake, *Earthquake Spectra* **29**, S219–S243.
- Oth, A., Bindi, D., Parolai, S., and Di Giacomo, D., 2011. Spectral analysis of K-NET and KiK-net data in Japan, Part II: On attenuation characteristics, source spectra, and site response of borehole and surface stations, *Bull. Seism. Soc. Am.* **101**, 667–687.
- Petersen, M. D., Frankel, A. D., Harmsen, S. C., Mueller, C. S., Haller, K. M., Wheeler, R. L., Wesson, R. L., Zeng, Y., Boyd, O. S., Perkins, D. M., Luco, N., Field, E. H., Wills, C. J., and Rukstales, K. S., 2008. *Documentation for the 2008 Update of the United States National Seismic Hazard Maps*, Open-File Report 2008–1128, U.S. Geological Survey.
- Rodriguez-Marek, A., Bay, J. A., Park, K., Montalva, G. A., Cortez-Flores, A., Wartman, J., and Boroschek, R., 2010. Engineering analysis of ground motion records from the 2001 Mw8.4 Southern Peru earthquake, *Earthquake Spectra* **26**, 499–524.
- Scasserra, G., Stewart, J. P., Bazzurro, P., Lanzo, G., and Mollaioli, F., 2009. A comparison of NGA ground motion prediction equations to Italian data, *Bull. Seism. Soc. Am.* **99**, 2961–2978.
- Scherbaum, F., Cotton, F., and Smit, P., 2004. On the use of response spectral reference data for the selection and ranking of ground motion models for seismic hazard analysis in regions of moderate seismicity: The case of rock motion, *Bull. Seism. Soc. Am.* **94**, 2164–2185.
- Shao, G., and Ji, C., 2011. Rupture characterizations of the 2011 Mw 9.1 off the Pacific coast of Tohoku earthquake and its March 9th Mw 7.4 foreshock constrained by an unprecedented data



- set for subduction earthquakes, Abstract U34A-03 presented at *2011 Fall Meeting, AGU*, San Francisco, CA.
- Si, H., and Midorikawa, S., 2000. New attenuation relations for peak ground acceleration and velocity considering effects of fault type and site condition, *Proc. World Conf. Earthquake Eng.*, Auckland, NZ, Paper 0532.
- Simons, M., Minson, S. E., Sladen, A., Ortega, F., Jiang, J. L., Owen, S., Meng, L. S., Ampuero, J. P., Wei, S. J., Chu, R. S., Helmberger, D. V., Kanamori, H., Hetland, E., Moore, A. W., and Webb, F. H., 2011. The 2011 magnitude 9.0 Tohoku-oki earthquake: Mosaicking the megathrust from seconds to centuries, *Science* **332**, 1421–1425.
- Skarlatoudis, A., and Papazachos, C. B., 2012. Preliminary study of the strong ground motions of the Tohoku, Japan, earthquake of 11 March 2011: Assessing the influence of anelastic attenuation and rupture directivity, *Seism. Research Ltrs.* **83**, 119–129.
- Stewart, J. P., Douglas, J., Javanbarg, M. B., Di Alessandro, C., Bozorgnia, Y., Abrahamson, N. A., Boore, D. M., Campbell, K. W., Delavaud, E., Erdik, M., and Stafford, P. J., 2013. Selection of ground motion prediction equations for the Global Earthquake Model, *Earthquake Spectra*, accepted, DOI: 10.1193/013013EQS017M.
- Wakamatsu, K., and Matsuoka, M., 2008. Development of national topography and site condition map with 250-m mesh size, *Annual Meeting of Japan Association for Earthquake Engineering, 2008.11*, 222–223 (in Japanese).
- Wei, S., Graves, R., Helmberger, D., Avouac, J. P., and Jiang, J., 2012. Sources of shaking and flooding during the Tohoku-Oki Earthquake: a mixture of rupture styles, *Earth Planet. Sci. Lett.*, in press.
- Yokota, Y., Koketsu, K., Fujii, Y., Satake, K., Sakai, S., Shinohara, M., and Kanazawa, T., 2011. Joint inversion of strong motion, teleseismic, geodetic, and tsunami data sets for the rupture process of the 2011 Tohoku earthquake, *Geophys. Res. Lett.* **38**, L00G21, doi:10.1029/2011GL050098.
- Zhao, J. X., 2011. Personal communication.
- Zhao, J. X., Zhang, J., Asano, A., Ohno, Y., Oouchi, T., Takahashi, T., Ogawa, H., Irikura, K., Thio, H. K., Somerville, P. G., Fukushima, Y., and Fukushima, Y., 2006. Attenuation relations of strong ground motion in Japan using site classification based on predominant period, *Bull. Seismol. Soc. Am.* **96**, 898–913.

(Received 1 April 2012; accepted 30 November 2012)